Resource-Efficient Technologies 3 (2018) 19–36

Resource-Efficient Technologies

journal homepage: http://reffit.tech/index.php/res-eff

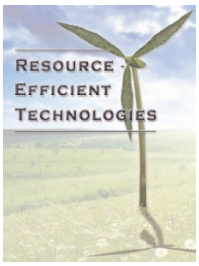

Research Paper

INTERACTION OF METALS AND ALLOYS WITH GAS MEDIA UNDER SPARK DISCHARGES

D.V. Mironov[1]*, V.M. Mironov[1], V.F. Mazanko[2], D.S. Gertsriken[2], P.V. Peretyatku[3]

[1] Samara State Agricultural Academy, Ust-Kinelsky urban village, Samara region, 446442, Russia
[2] G.V. Kurdyumov Institute for Metal Physics, NAS of Ukraine, Kiev, UA-03142, Ukraine
[3] Baltsy State Pedagogical Institute, Baltsy, Moldova

Abstract

The paper studies the penetration of nitrogen, oxygen, hydrogen, carbon, argon and krypton into copper, nickel, molybdenum, titanium, aluminum, iron and different steels under the action of spark discharges in various media based on radioactive indicators using step-by-step radiometric analysis, macro-, micro-, electron-microscopy and activation autoradiography, Mössbauer and Auger spectroscopy, secondary ion-ionic emission, X-ray diffraction and X-ray microanalysis.

The study describes distribution features of penetrating atoms and their concentration profiles. Phase composition of near-surface layers is also determined. It is shown that supersaturated solid solutions of iron in copper and copper in iron are formed during simultaneous iron and oxygen penetration in copper and spinel $(Fe_6Cu_3O_4)_4$. Diffusion of iron and carbon results in supersaturated solid solutions of iron and carbon in copper, copper and carbon in iron, graphite and cementite. Inert gases and nitrogen form solid solutions with copper.

Phase composition of near-surface layers in Fe is determined. Iron dioxide FeO, a carbon solid solution in iron with fcc lattice γ-Fe, tetragonal martensite and cementite, two iron (III) hydroxide FeOOH modifications, a supersaturated solid solution of nitrogen and nitride Fe_4N, solid solutions of inert gases in iron are formed in the diffusion zone.

Simultaneous interaction of molybdenum with iron (the anode material) and various gases results in the formation of substitutional solid solutions of iron in molybdenum and molybdenum in iron, a small amount of interstitial solid solutions of nitrogen and carbon in molybdenum and nitrogen in iron, interstitial phases: molybdenum nitrides and carbides and traces of nitrides of iron (Fe_4N, Fe_2N) and $Fe_{1,9}Mo$ (λ) phases in the form of needles.

Treatment of nickel with a nickel anode in the nitrogen medium promotes formation of a solid solution of nitrogen and nitride Ni_3N in the matrix with preserved hexagonal symmetry and lattice parameters that are characteristic of this phase under equilibrium conditions. Atoms of oxygen, nitrogen, carbon and argon are present in the interstitial solid solutions in treatment of nickel in ambient air; however, oxides are not found even on the surface (in the layer ~200 nm).

Interaction of titanium with atmospheric gases leads to formation of a solid solution of nitrogen, oxygen, carbon, hydrogen and argon in titanium and titanium nitride Ti_2N (ε). Simultaneous saturation of the titanium surface with nickel and nitrogen in the interaction zone causes formation of phases in the following order: nickel nitride; a solid solution of nitrogen and titanium in nickel and a solid solution of both alloying elements in titanium.

Key words: spark discharge, electrospark alloying, concentration profile, phase composition.

* Corresponding author: Samara State Agricultural Academy,
Ust-Kinelsky urban village, Samara region, 446442, Russia.
E-mail address: dvonorim@mail.ru

Peer review under responsibility of Tomsk Polytechnic University.
https://doi.org/10.18799/24056537/2018/3/199

1. Introduction

In contrast to high-energy ion beam irradiation of metals, spark discharge plasma (glow, arc and spark discharges) in different gas media causes not only incorporation of media ions into the near-surface layer to the depth of the projective range, but also their further migration deep into metal [1–7]. This effect changes phase composition on the surface of the material and at considerable depths [2–7], and the structure and properties of metallic products [3, 4]. However, until now, undesirable effects of the penetration of atmospheric constituents into metals have been studied insufficiently. Therefore, it seemed expedient to consider the interaction of metals with atoms and molecules of the air or neutral media during electrospark treatment, since when impurities are doped into metals through spark discharges, the treatment is carried out in the air or in neutral media. Similar studies are currently being conducted, sometimes purposefully and in some cases incidentally; a number of results have already been obtained [7–10]. This study is a generalization of previously obtained and original scientific findings.

2. Materials and methods

2.1. Materials

The experiments were conducted on metals that were pre-annealed for 1 h: monocrystalline molybdenum (99.999 % Mo) (2173 K); high-purity copper (99.99995 % Cu) (1073 K); electrolytic nickel (99.99 % Ni); ultra pure single-crystal aluminum AB 000 (99.99995 % Al); α-titanium and BT20 titanium alloy; ingot iron (99.8 % Fe) and steels 3, 20, 45 (1573 K), copper alloys with 10–30 % Ni and homogeneous iron alloy with 30 % Ni in the γ-state (fcc lattice). The samples were shaped as a parallelepiped 10×10×5 mm in size. The working surface (10×10 mm) was prepared so that the microroughness value determined by the profilograph did not exceed 0.05 μm. After electropolishing, the surfaces of all metals except molybdenum were etched to reveal their grain structure. For copper, the etchant composition was as follows: 100 ml of 3 % hydrogen peroxide H_2O_2, 5 ml of concentrated sulfuric acid H_2SO_4, distilled water in the amount to attain the volume of 1: l. Etching was carried out for 60–90 s at room temperature. For iron etching, a 5 % aqueous or alcoholic solution of nitric acid HNO_3 was used. The etching time was 60–90 s. For chemical etching of titanium, an etchant was of the following composition: hydrofluoric acid HF – 80 ml and HNO_3 – 140 ml per liter of distilled water. Etching was performed for 20 s at room temperature. For nickel, an etchant was of the following composition: nitric acid – 2250 ml, sulfuric acid – 1500 ml, sodium chloride – 30 g and water – 1000 ml. The solution temperature was 293 K, and the treatment time was 5–10 s. Aluminum was etched in a 8–10 % sodium hydroxide solution at 323–353 K for 1–2 min.

Electrospark treatment of metals was carried out in various media in humid air; in the air that contained small ^{14}C-labeled carbon dioxide additives; water vapor containing tritium ^{3}H, or ^{85}Kr radioactive isotope; in the medium of carbon dioxide CO_2 and $^{14}CO_2$, purified nitrogen, argon and argon with additives of the radioactive krypton isotope ^{85}Kr. The experiments were conducted in sealed chambers to work with atmospheric radioactive isotopes. The anodes for electrospark alloying (ESA) were made from metals of equal purity, alloys of equal and different composition, and pyrolytic graphite. For the experiments with multiphase systems, the anode consisted of multicomponent nickel-chromium alloy VGL (60 % Ni, 20 % Cr, 10 % Fe, 5 % Mo, 2.5 % Ti, 1.4 % Al, 0.5 % Mn, 0.5 % Si, 0.07 % C, 0.02 % P and 0.01 % S), which is an interstitial and substitutional solid solution based on nickel with the fcc lattice. In some studies, the anodes contained radioactive and stable isotopes ^{44}Ti, ^{57}Fe, ^{55}Fe, ^{63}Ni, ^{67}Cu, ^{99}Mo and ^{14}C. The following electrolyte was used to deposit galvanic iron coating – radioactive (^{55}Fe) or stable isotope (^{57}Fe) – on the iron anode that consisted of ^{56}Fe atoms: 500 mg/ml $FeCl_2 \cdot 4H_2O$, 250 mg/ml NaCl, 3 mg/ml HCl, and 2–3 drops of a saturated $FeCl_3$ solution with corresponding isotope (^{55}Fe or ^{57}Fe) labeling. The radioactivity of the electrolyte with ^{55}Fe atoms did not exceed 10 mC. Nickel plating was carried out in a weak electrolyte of the following composition: nickel sulphate $NiSO_4$ – 140 g, sodium sulfate Na_2SO_4 – 50 g, magnesium sulfate $MgSO_4$ – 30 g, sodium chloride NaCl – 5 g, boric acid H_3BO_3 – 20 g and water – 1000 g. The electrolyte temperature ranged from 291 to 298 K and the current density was 0.8–1 A/dm^2. The quality of the coating depends largely on the electrolyte acidity (pH); therefore pH was adjusted to 4–5 by adding a small amount (drops) of an aqueous solution of ammonia. A nickel layer of up to 1 mμm thickness settled within 20 minutes at a current density of 0.15 A/dm^2, and within 30 min at 0.1 A/dm^2. The radioactive isotope ^{63}Ni was poured into the finished electrolyte in the amount of several drops of $NiSO_4$-labeled nickel. The following electrolyte was used to apply copper coating: copper sulfate ($CuSO_4$, including ^{67}Cu-labeled copper sulfate) – 200 g, concentrated sulfuric acid H_2SO_4 – 30–50 g and water – 1000 g. The electrolyte temperature was 291–298 K and the current density was 1–2 A/dm^2. The layer was applied within no more than 1–2 min.

The titanium surface was successively subjected to chemical degreasing, drying, sandblasting with

electrocorundum No. 10 and hybrid treatment in $HCl–H_2SO_4$ mixture at the ratio of 1:1 to apply a 10–40 μm nickel-phosphor coating on titanium. Next, chemical nickel plating was carried out at T=360–365 K for 2–3 h in the solution of the following composition: 20–30 g/l $NiSO_4$, 20–25 g/l of sodium hypophosphite $NaHPO_2$, 20–25 g/l of aminoacetic acid (glycine) NH_2-CH_2-COOH, 14–17 g/l of sodium acetate, CH_3-COONa and 0.002–0.003 mg/L of ethyl urea $C_3H_8N_2O$. The formed coating consisted of a supersaturated solution of phosphorus in nickel. After 1 h annealing at 573–623 K, two phases appeared: a solid solution of phosphorus in nickel (fcc lattice) and ~15 % of finely dispersed (less than 0.05 μm) nickel phosphide Ni_3P of tetragonal symmetry. The diffusion zone between the coating and the substrate at these low temperatures and short times amounted to hundredths of a micron.

To incorporate ^{14}C radioactive carbon into the iron anode, cementation was carried out in a solid (powder) carburizing agent $Ba1^4CO_3$ at 1273 K for 1 h. The radioactivity on the carburized iron anode surface was more than 1 mC. The surface layer of carbon-saturated iron with a thickness of ~10 μm consisted of a solid solution of carbon in α-iron and iron carbide Fe_3C in about equal amounts. Saturation of iron with stable carbon was performed under similar conditions (annealing temperature of 1273 K, annealing time of 1 h, carburizing agent $BaCO_3$, but without labeled carbon atoms). The radioactive nitrogen isotope ^{13}N was produced directly in the sample by nuclear reaction $^{14}N+^0n\rightarrow{}^{13}N+2^0n$. Activation was carried out by neutron irradiation of stable nitrogen atoms found in the sample after their incorporation into the sample by spark discharges in nitrogen medium ^{14}N. Argon atoms doped into the sample by spark discharges in stable argon medium ^{40}Ar were activated in a similar manner. The reaction used to produce labeled argon atoms ^{41}Ar from stable argon was $^{40}Ar+^0n=^{41}Ar+\gamma$. Only one type of isotope, including nitrogen or argon isotopes activated in the reactor, was used in each experiment conducted with radioactive isotopes. The characteristics of the radioactive substances [11, 12] are summarized in Table 1.

2.2. Electrospark treatment

An industrial apparatus [13] was used for electrospark treatment of samples and deposition of coatings. The apparatus consists of a pulse current generator and a loading unit (Fig. 1). Spark discharges are generated between two electrodes (the cathode is the treated product, and the anode is the material used for alloying of the treated surface) exposed to voltage supplied from the generator. The spark discharge energy varied in the range W~0.9–6.4 J. The discharge pulse repetition rate was ν>60 Hz. The pulse duration τ_i was 200 μs. In the experiments, both a conventional (contact) method and a noncontact alloying method were used. The value of the electrode gap EG l varied from 0.5 to 2 mm. The experiments were conducted in a purpose-built chamber, where appropriate media were introduced.

Table 1. *Features of the radioactive isotopes*

Isotope	Decay mode	Half-life period	Energy of β-particle, γ-quantum energy and characteristic X-radiation, keV
^3H	β^- (electrons)	12 years	10 (β)
^{13}N	β^+ (positrons)	10 minutes	1500 (β)
^{14}C	β^-	5 000 years	150 (β)
^{26}Al	β^+, ε (electron capture)*	720 000 years	3 000 (β), 1120 (X-rays)
^{41}Ar	β^-, γ	110 minutes	2500 (β), 1500 (γ)
^{44}Ti	ε	60 years	75.3 (X-rays)
^{55}Fe	ε	3 years	52 (X-rays)
^{63}Ni	β^-	125 years	65 (β)
^{67}Cu	β^-	2.2 days	189 (β)
^{85}Kr	β^-, γ	10 years	680 (β), 517 (γ)
^{99}Mo	β^-	2.8 days	1230 (β)

** electron capturing by nucleus, typically from 1S (K) or 2S (L) level of the electron shell of an atom that results in the emission of characteristic X-radiation of the atom element formed after electron capturing*

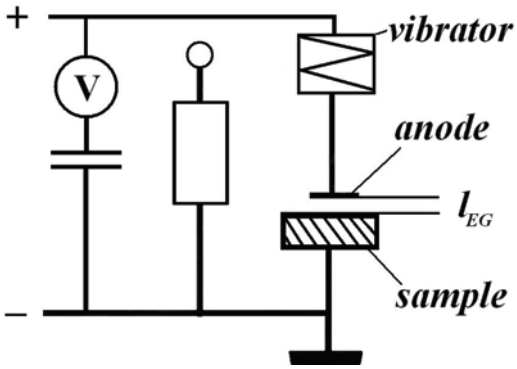

Fig. 1*. Apparatus for spark discharge treatment*

Atomic diffusion, the features of the localization of penetrating atoms and changes in the phase composition on the surface of the treated metals and in the transition zone between the coating and the matrix were studied using a set of standard methods based on various principles [14–31]. This provided not only the reliability of the results obtained, but also a variety of data on phase formation processes, which cannot be obtained by one particular method. Some of these methods can disclose the process of atom displacement and the formation of new phases, other methods can be used to determine their crystal structure and morphology, some other methods identify their chemical composition or show the features of their localization. Different methods of investiga-

tion, primarily those involving the use of radioactive isotopes, were used to identify the shape of the concentration profile for penetrating atoms [14–24].

Radioactive indicators were employed to study the process of redistribution of atoms to plot a concentration curve for isotope depth distribution. In this regard, the method of layer removal with a 0.5–0.7 μm step was used to determine the integral radioactivity of the remaining part of the sample after removal of the material layer (the Gruzin's method [14]). Macroautoradiography was another method used for large penetration depths [15]. To study the structural, concentration and chemical inhomogeneities in both the surface layers and the bulk of the metal layers, well-known methods of microautoradiographic [16–19] and electron microscopic autoradiography were used, including activation autoradiography [20–24]. The distribution of penetrating atoms in the coating and bulk material was estimated by the method of secondary ion mass spectroscopy (SIMS) using a microscanner [25]. Other methods used to determine the shape of the concentration profile were as follows: micro-X-ray spectral analysis [26] using the Cameca spectrometer, metallography (with x 500–2000 magnification), layered X-ray diffraction analysis with ~15 μm step (using chromium K-radiation: λ_{α_1}=0.22896 nm, λ_{α_2}=0.22935 nm and λ_{β_1}=0.20848 nm) with an error of the interplanar distance determination and grating periods not less than 0.00003 nm [27] and microdurometry. Conversion electron Mossbauer spectroscopy [28], Auger electron spectroscopy [29] and scanning electron microscopy [30] were used to determine phase composition.

3. Results

The experiments conducted on copper samples showed that ESA without heating in the described medium stimulated penetration of carbon atoms into copper similar to that occurring under glow discharge generated in a methane medium [32] (Fig. 2). Two sources of ionized carbon, the medium and the dispersing electrode increased the concentration of penetrating atoms (Curve 2) as compared to that observed when atoms were doped from the medium only (curve *1*).

Under spark discharges, labeled copper atoms from the pre-dispersed coating or from the anode material containing ^{67}Cu atoms penetrated to the same depth, which is of the order of 20 μm. The concentration profile starting with 3–4 μm is described by the exponential dependence on the squared penetration depth. However, it should be noted that under these loading conditions, but in the methane medium without labeled carbon atoms, ^{55}Fe iron atoms penetrated into copper (from the iron electrode) to a much greater depth of up to 30 μm.

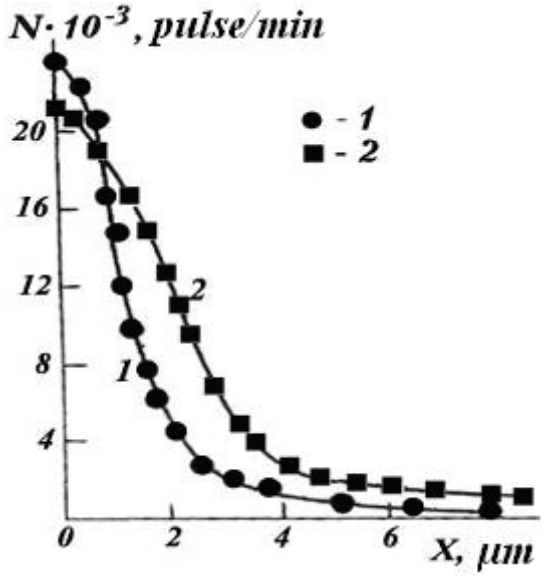

***Fig. 2**. Distribution of ^{14}C in copper during ESA in $^{14}CH_4$ methane medium by copper (1) and carbon electrode containing ^{14}C (2), W=3.4 J, τ_1=200 μs, contact treatment*

The analysis of the diffusion zone phase composition showed that both schemes used for doping of carbon into copper provided not a mechanical mixture of carbon and copper but a solid solution, and the copper lattice parameter distinctly reduced (from 0.3615 to 0.3609 nm). Consequently, it can be assumed that some of carbon atoms replaced copper atoms at the lattice sites, although the difference in atomic radii of copper and carbon exceeds 15 %. Isothermal annealing at 973 K for 1 h caused disintegration of the metastable solution, escape of carbon atoms from the bulk to the surface and formation of a thin (~0.1 μm) graphite layer of hexagonal symmetry. The lattice parameters *a* and *c* were identical to the data reported in [27]. The copper lattice parameter returned to its initial value and the autoradiograms-replicas (after removal of the graphite layer) showed no reduced AgBr crystals even in case of long exposures.

Simultaneous penetration of carbon from the medium (CO_2) and iron from the electrode into copper also caused formation of a metastable solution. Upon heating, it decayed with the release of carbon and formation of dispersed iron clusters in the diffusion zone. Let us consider these results in more detail.

The X-ray patterns of copper samples saturated with iron and carbon obtained using chromium K?a radiation indicate the lines of a solid carbon and iron solution in copper (κ-Cu), broadened lines of copper and a carbon solid solution in iron (α-Fe) with an intensity of 3–4 fold smaller than that of reflections from the copper crystallographic planes, which insignificantly differ from the background of the second line of graphite line (H9 according to the classification provided in [27]) and several lines of orthorhombic cementite Fe_3C, mainly at small

angles, where the background is minimal (Table 2). It should be noted that the tetragonality of martensite formed in iron during carbon dissolution is so small that the doublets of X-ray reflections do not split, but form diffuse lines. The calculated carbon concentration in the solution with respect to the width of the α-iron line (110)–(011) [31] attains ~0.5 %.

The calculation of the crystal lattice parameters of the formed *a* phases has shown that mutual dissolution considerably affects these parameters. Thus, as a result of dissolution of carbon and iron in copper, the value a_{Cu} decreased by 0.0225 nm and amounted to 0.33741 nm. It should be noted that under steady-state conditions at room temperature, the mutual solubility of iron and copper is extremely small (<10^{-6} % at.) [33]. Dissolution of carbon and copper in iron increased the lattice parameter. The value a_{Fe} grew by 0.0075 nm and amounted to 0.3015 nm. A complex solid solution was formed in iron – copper atoms at the lattice sites where they replaced iron atoms, and carbon atoms were in tetrahedral and octahedral pores, i.e. in interstitial positions. Micro-X-ray spectral analysis showed up to 30 % of iron dissolved in copper and more than 10 % of copper dissolved in iron. Consequently, it can be assumed that dissolution in bulk material is more intensive than that in the formed coating. However, strong difference in the amount of solute in copper and iron may be due to the effect of carbon, more specifically, to some loosening of the copper lattice when carbon atoms form a solid solution by substitution, while in iron carbon forms a solid interstitial solution.

After annealing (973 K, 1 h), the parameters of the crystal lattices of copper and iron return to initial values, since metastable solutions decay.

Table 2. *Phase composition of the coating, transition zone and matrix recorded using chromium K-radiation* λ_{α}^{Cr}*=0.22909 nm* λ_{β}^{Cr}*=0.20848 nm*

$2\theta^0$	*d*, nm	λ	(h k l)	*I*, %	Phase
39.6	0.3380	α	012	5	C (carbon)
57.5	0.2380	α	021	8	Fe_3C
60.8	0.2261	α	200	5	Fe_3C
62.3	0.2213	α	120	5	Fe_3C
64,617	0.19502	β	111	9	κ-Cu
65.0	0.2132	α	110	12	α-Fe
66.0	0.2104	α	121	6	Fe_3C
67.4	0.2065	α	013	5	Fe_3C
69.8	0.2001	α	103	10	Fe_3C
71.931	0.19503	α	111	100	κ-Cu
76.321	0.16871	β	200	4	κ-Cu
85.522	0.16871	α	200	50	κ-Cu
93.3	0.1575	α	200	8	α-Fe
121.815	0.11930	β	220	6	κ-Cu
137.0	0.1231	α	211	9	α-Fe
138.0	0.1227	α	$0\bar{2}\bar{2}$	1	C
147.571	0.11929	α	220	70	κ-Cu

However, the shape of the X-ray reflections is different: the observed thin copper lines and broadened iron lines are apparently related to high dispersion of iron precipitates. The value of the half-width *B* of the copper line (111) did not exceed $1.7\cdot10^{-3}$ rad, and the value of *B* for reflection from the iron plane (110) was $3.6\cdot10^{-3}$ rad. Before annealing, i.e. after spark discharges, B_{Cu} was $1.9\cdot10^{-3}$ rad, and B_{Fe} was equal to $2.7\cdot10^{-3}$ rad. After annealing, the intensity of the iron lines increased 2.5-fold, since the amount of iron grew. The intensity of the reflections from cementite and graphite also increased (1.3–1.6-fold) but the interplanar distances *d* did not change. Consequently, these phases grew with no change in their composition. No new phases appear in the diffusion zone, matrix and coating.

During ESA of copper with iron in ambient air (*W*=0.9 J, τ_l =200 μs, $t_{treatment}$=1 min/cm^2), the surface layer of the sample up to 30 μm thick, i.e. the coating itself and the transition zone between the coating and the substrate, is a solid solution of copper, nitrogen, oxygen, carbon, argon in iron, the solution of the above elements in copper and ordered iron nitride Fe_4N (γ'-phase). This phase retains the symmetry inherent in the formation under equilibrium conditions and exhibits a face-centered cubic lattice (fcc lattice). However, the fcc lattice parameter is 0.3811 nm, which considerably exceeds the equilibrium conditions a_{max}=0.3801 nm [Ko]. Since the ordering of the γ'-phase in the solid solution was experimentally proved, the exceeded lattice parameter, as compared to that reported in literature, is most probably caused not by the excess of nitrogen, but by the penetration of copper atoms into the formed coating.

The coating composition is given below:

Element	Fe	Cu	N	O	Ar	C	Pairs H_2O
C, % at.	51	25	13	10	≤1	traces	traces

In contrast to nitrogen, oxygen atoms penetrated into the metal from medium are found in the solid solution only and are not bound to oxides or hydroxides according to the data obtained by Mössbauer spectroscopy and X-ray diffraction analysis.

The study of the interaction of copper with an iron coating in the air during electrospark treatment using harder modes showed that the surface layer ~40 μm thick was an iron-copper solid solution containing 57 % at. Fe and 32 % at. Cu (Fig. 3). In addition, the coating contained up to 11 % at. oxygen not bound to iron oxides. This considerable amount of oxygen cannot dissolve in the lattice of a substitutional solid solution of iron-copper; therefore, oxygen is supposed to play the main role in formation of the amorphous phase, since the Mössbauer spectra exhibited neither iron oxides nor iron hydroxides. However, simultaneous formation of amorphized phases and

spinels of $(Fe_6Cu_3O_4)_4$ type is more likely to occur. Under steady-state conditions, no phases of this type were observed.

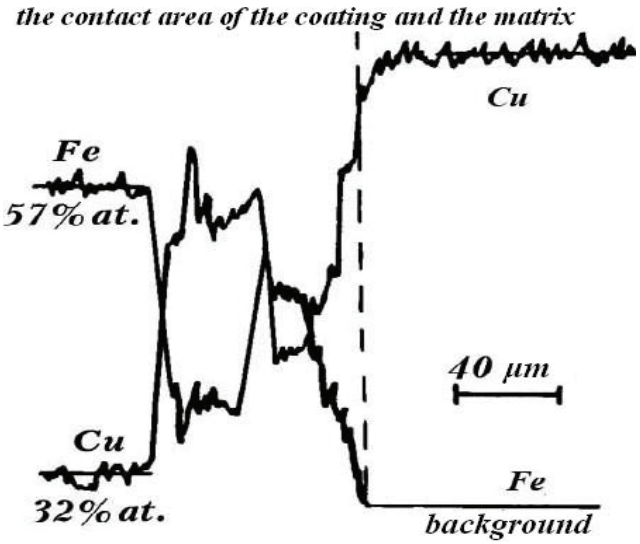

Fig. 3. *Concentration distribution curves for Fe and Cu in the coating under ESA of copper with iron (W=3.4 J, τ_I=200 μs, $t_{treatment}$=1 min)*

In contrast to dissolution of carbon in copper, the lattice parameter of the inert gas solid solution in copper increases during alloying of argon atoms (copper anode, medium is argon or argon with additives of ^{85}Kr radioactive isotope). For treatment parameters W=6.4 J, τ_i=200 μs and n_i=5·10^4, the value a in the near-surface layer up to 15 μm (the assumed region of data acquisition when using chromium K_α radiation) attains 0.3620 nm and the penetration depth determined by diffusion of labeled krypton atoms is 25 μm. However, the electron microscopic autoradiographic data show that no krypton atoms can be virtually observed on the surface or, more precisely, in the ~2 μm layer. This is apparently caused by gas release due to high temperature on the surface. That is, each discharge causes incorporation of atoms into copper, diffusion deep into copper and insignificant thermal desorption from the surface. It should be noted that glow discharge treatment provides these concentrations of dissolved atoms and penetration depths at much higher energies of bombarding ions and longer exposure time [32].

In transition from copper to a solid solution of nickel in copper, the above treatment parameters cause reduction of argon and krypton penetration depth to ~20, ~16 and ~13 μm as nickel concentration increases from 10 to 30 μm with a 10 μm step. At the same time, no differences in the mobility of atoms of both elements were detected. It should be noted that increased concentration of nickel dissolved in copper during glow discharge treatment has a stronger inhibitory effect on inert gas transfer [32].

The direct effect of spark discharges (without electrode gap) (W=3.4 J, τ_i=200 μs, l_{EG}=0, specific treatment time t=1 min/cm^2) on the copper sample (copper anode) in the air increases the copper lattice parameter by 0.00052 nm. In this case, a complex interstitial solution is formed. It should be noted that the copper crystal symmetry does not change and no phases other than a solid solution can be observed. These results differ somewhat from those obtained using the same equipment with a similar spark discharge effect on copper in the air. The increment in the copper lattice parameter (Δa=0.0004 nm) and some traces of an unidentified phase were found to be smaller. This may be due to both a lower discharge energy (1 J), which provides smaller penetration of nitrogen and oxygen atoms into the metal [34], and a nickel anode used. The size of nickel atoms is smaller than that of copper atoms; therefore, their dissolution reduces the increment value Δa that occurs when nickel atoms and light elements (nitrogen, oxygen) penetrate into copper simultaneously. In addition, we suppose that unidentified reflections in X-ray diffraction patterns can be the reflections from the nickel-based compound. Considering the differences in the interaction of copper with light elements caused by dissolution and diffusion of nickel, and the presence of water vapor, carbon dioxide, argon, etc. in the air in addition to nitrogen and oxygen, the results obtained in this study indicate the possibility of incorporation of almost any non-metal atoms in large quantities into copper.

The experiments were carried out in a purified nitrogen medium using a copper anode in order to study interaction of copper directly with nitrogen. In this case, the copper lattice parameter also sharply changed and increased from 0.00042 to 0.00056 nm with an increase in W varying from 0.9 to 6.4 J (τ_i=200 μs, the specific treatment time of 1 min/cm^2). Comparison of the copper lattice parameter when treated in nitrogen medium and in the air shows that the penetration of nitrogen atoms causes a greater change in α than that of atoms and molecules of the remaining atmospheric constituents.

The SIMS method used to study the shape of the concentration profile of the nitrogen distribution in copper under these treatment conditions showed that the nitrogen concentration maximum appeared at ~250 to 300 nm from the surface of the formed coating (Fig. 4).

After reaching the maximum, the depth concentration of nitrogen in copper decreases exponentially. Consequently, it can be assumed that in glow discharge [32, 34], a supersaturated layer of a nitrogen solid solution in copper is initially formed and then nitrogen atoms diffuse into copper from this layer similar to what can be observed when bombarding

with ions that are insoluble in metals under equilibrium conditions (nitrogen and carbon in copper, helium and argon in aluminum, krypton and xenon in iron, etc.).

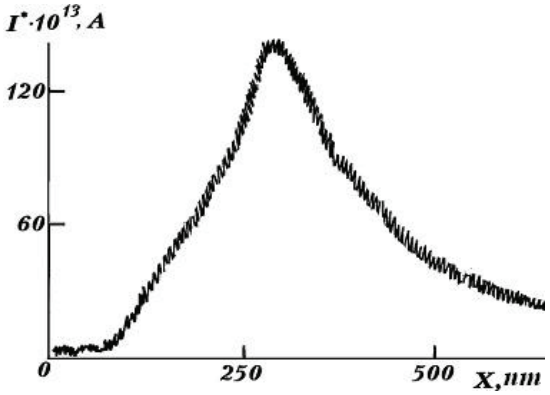

Fig. 4. *Change in the concentration of nitrogen (secondary ion current of nitrogen) in copper versus the penetration depth, 3.4 J, 200 mμs, 1 min/cm²*

Annealing of copper saturated with both nitrogen and atmospheric constituents at 973 K for 1 h results in the initial level of *a* equal to 0.36143 nm. That is, nitrogen and oxygen are assumed to form a solid solution that decomposes upon heating similar to carbon. Substances insoluble under equilibrium conditions can be incorporated into copper to form a solid solution; however, when heated, the solid solution formed during electrospark treatment disintegrates.

Figs. 5–6 demonstrate interaction of iron with air gases during spark discharge. The microautoradiogram in Fig. 5a shows that the incorporation of hydrogen atoms (tritium) from water vapor into iron causes formation of phase clusters located mainly near the grain boundaries on its surface.

The autoradiographic pattern of the surface, that is, the distribution of labeled hydrogen atoms, is practically similar for contact and non-contact treatment techniques. It could be assumed that these treatment conditions cause iron hydride formation. However, Mössbauer spectroscopy showed that this phase is ferric hydroxide, which is formed by contact and non-contact treatment.

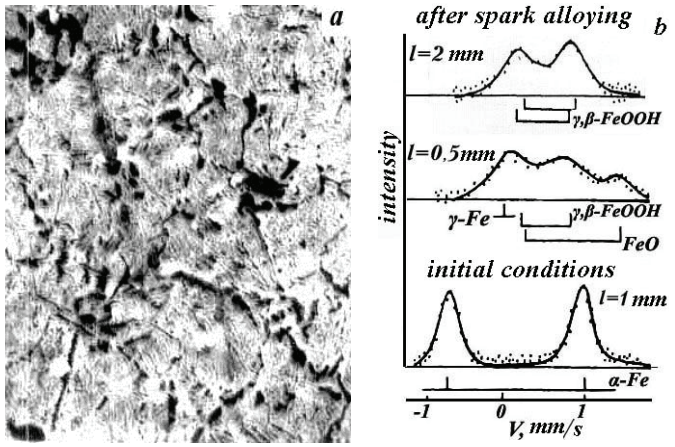

Fig. 5. *Distribution of ³H atoms in iron after contact treatment at the energy W = 4.5 J. (a is microautoradiogram, x 500 magnification) and phase composition of iron after contactless spark discharge treatment (W=4.5 J) and in the initial state (b is Mossbauer spectra of the samples, ⁵⁷Fe)*

The Mössbauer spectra show (Fig. 5b) that the phase composition of the surface and the penetration depth of atmospheric gases depend on the EG value. If l_{EG}=0.5 mm, highly dispersed phases of ferrous oxide FeO, a carbon solid solution in iron with a fcc lattice γ-Fe and two modifications of ferric hydroxide FeOOH arise on the iron surface. The carbon solid solution in iron with a fcc lattice γ-Fe does not have time to transform from high-temperature γ-modification to low-temperature α-modification due to an ultrahigh cooling rate of up to 10^6 deg/s. It should be noted that concentration of the γ-phase is sufficient for its detection by X-ray diffraction. The presence of the γ-phase is associated with the anode-cathode transfer of carbon in the amount sufficient for its formation. As will be shown below, if l_{EG}=2 mm, no γ-phase is formed, which is apparently due to a lesser depth and, hence, lower concentration of the penetrated substance. Thus, the penetration depths of ^{14}C atoms from $^{14}CO_2$ in the first case are X~7–7.5 μm and in the second case they attain no more than 2 μm.

Data obtained by Auger spectrometry shows that N, O and C atoms penetrate deep into iron (Fig. 6) and form different concentration profiles.

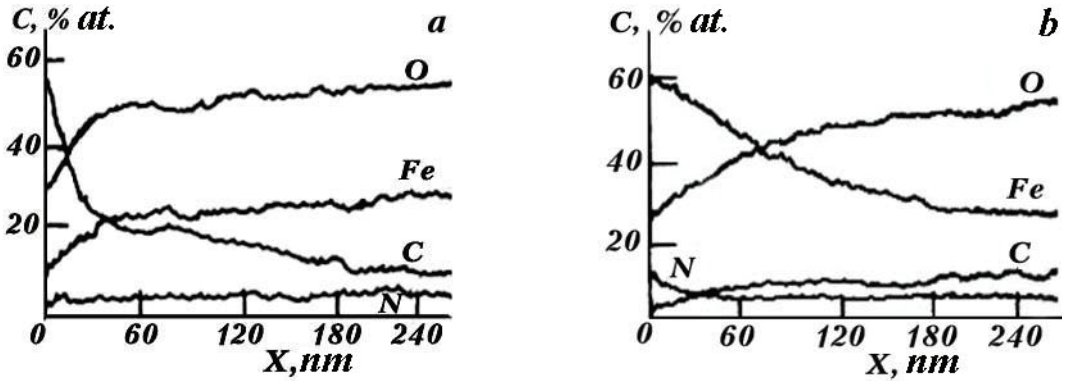

Fig. 6. *Distribution of different elements in iron, W=4.5 J, iron anode l_{EG} is 0.5 (a), 2 mm (b), Auger spectroscopy*

Distribution of iron, oxygen, carbon and nitrogen in the sample at l=0.5 mm shown in Fig. 6a indicates that carbon accumulates in the surface layer. Its concentration decreases rapidly as it penetrates deep into the sample and oxygen concentration reaches the value of 50 % at. High concentration of oxygen can be achieved by the formation of hydroxides in the sample surface layer. In addition, nitrogen (up to 5–6 % at.) is found in the surface layer (up to 300 nm). On the surface of iron and in the thin layer near the surface, the amount of carbon and oxygen atoms in austenite, oxides, hydroxides and in nitrogen is so high that iron atoms previously located on the surface are displaced into the metal at the distance of the order of 60 nm. For example, in a ~20-nm layer, concentration of light elements reaches 90 %. It is interesting that concentration of nitrogen in iron near the surface is almost an order of magnitude lower than that of oxygen and carbon. This can be due to its much weaker interaction with iron, similar to what can be observed under equilibrium conditions.

When l increases to 2 mm, the main components of the surface layer are iron and oxygen, although carbon and nitrogen can be found as well (Fig. 6b). In this case, oxygen concentration reaches 60 % at. and appreciably decreases deeper in the sample, which may be due to the formation of hydroxides on the surface and the formation of metastable iron oxides in deeper layers, since X-ray diffraction data indicate no FeO on the sample surface (only paramagnetic iron oxide formed at room temperature). Therefore, we can conclude that thin Fe_2O_3 and Fe_3O_4 layers are metastable, as is known from [35]. The possibility of amorphous iron oxide formation is not excluded [36]. The complexity of the M?ssbauer spectra (Fig. 5b) complicates their unambiguous interpretation. However, the analysis of the main features allows to make a conclusion about the structure of the formed layer. Its effective thickness h can be determined by the ratio $h=kE/Sl$, where $E=\int_0^{\tau} U(t)\cdot I(t)dt$ is the energy generated in EG per unit discharge, U and I are the gap voltage and discharge current, respectively; τ is current pulse duration; S is the exposed area; l is the EG value; k is the constant of proportionality, which depends on the thermophysical constants of the treated material.

The results clearly show that spark discharge treatment causes anomalous oxygen saturation of the surface, which can be used to form a surface with specific properties. In addition, conditions for the material transfer from the anode to the cathode are critical relative to the EG value. At large distances, light components of the anode alloy are sputtered, which enables targeted formation of the surface layer phase composition.

Experiments were carried out in a purified nitrogen medium using an anode from iron containing ^{55}Fe radioactive isotope to study the penetration of nitrogen atoms (without impurities) into iron during spark alloying. The nitrogen atoms formed in $^{55}Fe_4N$ spark alloying were located mainly along grain boundaries (Fig. 7), whereas the nitrogen solid solution in iron and labeled iron atoms can be found inside the grains. Iron nitride and the nitrogen solid solution in iron retain the symmetry inherent in equilibrium – fcc and bcc, respectively. However, the ratio of components in nitride is different from the stoichiometric one – 1:3.8 was observed instead of 1:4. Consequently, nitride is formed with nitrogen deficiency.

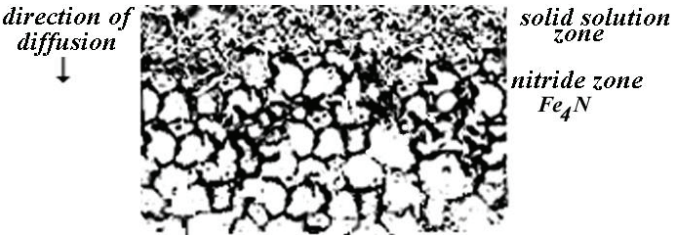

Fig. 7. *Microautoradiogram of iron saturated with stable nitrogen and ^{55}Fe isotope in alloying, x 500 magnification, W=3.6 J, τ_I=200 μs, τ=30 s, l_{EG}=0.5 mm*

The activation analysis (^{12}N) showed similar distribution of Fe_4N nitride phases with labeled nitrogen atoms along grain boundaries (Fig. 8). However, a significant amount of uniformly distributed nitrogen atoms can be found in the grain volume. Consequently, the nitrogen solid solution in iron occurs inside the grain, and iron nitrides can be observed along the grain boundaries in the metal.

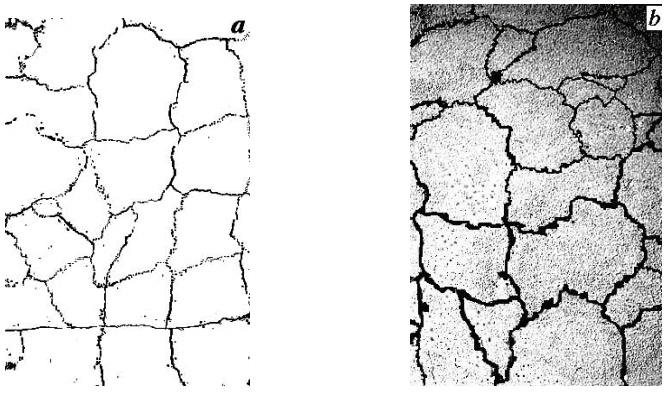

Fig. 8. *Microstructure (a) and microautoradiogram in the emission of activated nitrogen ^{12}N (b) of iron saturated with nitrogen in the mode W=2.4 J, τ_I=200 μs, τ=30 s, l_{EG}=2 mm, x 2,000 magnification*

Spark discharge treatment of the most widespread naturally occuring stable iron (97–98 % of ^{56}Fe and 2–3 % of ^{57}Fe) using a stable iron anode of the same composition in a carbon-labeled CO_2 medium and using an iron anode containing radioactive isotope ^{14}C in stable carbon dioxide gas showed similar

results. The autoradiograms were found to be similar (Fig. 9). In both cases, the labeled atoms were uniformly distributed inside the grains, and the interstitial phases were detected along the grain boundaries. X-ray diffraction analysis of carbon-alloyed iron produced using stable iron and carbon showed that highly dispersed fcc iron, Fe_3C cementite with carbon deficiency and a supersaturated solid solution of carbon in bcc iron (tetragonal martensite) were observed on the surface and in the diffusion zone. It should be noted that the concentration of the austenitic γ phase (^{14}C) and Fe_3C (^{14}C) carbides, and the penetration depth of ^{14}C atoms increase by a factor of 2 and 5, respectively, as the spark discharge energy grows from 0.3 to 6.4 J.

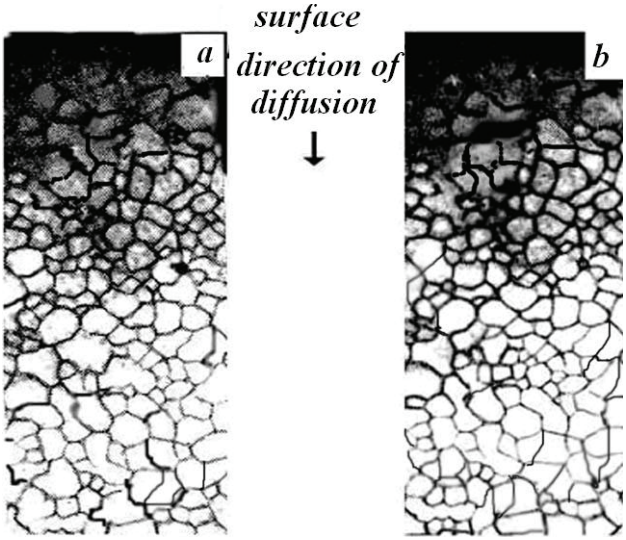

Fig. 9. *Penetration of ^{14}C carbon atoms into iron from the atmosphere (a) and from the anode (b), x 500 magnification, W=6.4 J, τ_I =200 μs, τ=2 min, l_{EG}=0.5 mm*

When inert gases (argon and krypton) were introduced into iron, the experiments were carried out in an argon medium or in argon supplied with radioactive isotope ^{85}Kr. In the first case, stable iron and isotope ^{85}Kr were employed. In the second case, the iron anode contained a small amount of ^{55}Fe radioactive isotope, and the atmosphere contained stable argon only. Autoradiographic and layerwise radiometric analysis revealed that both intrinsic atoms and atoms of inert gases penetrate into iron to macroscopic depths (Fig. 10).

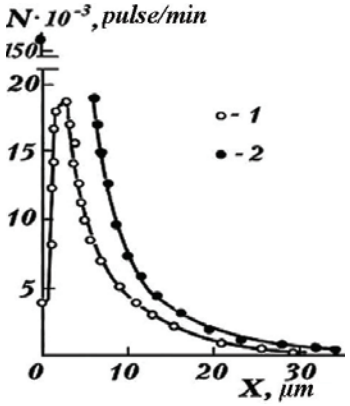

Fig. 10. *Distribution of ^{85}Kr atoms (from the atmosphere) (1) and ^{55}Fe atoms (from the anode) (2) in iron, W=0.9 J, τ_I=200 μs, τ=1 min, l_{EG}=0.5 mm*

It should be noted that a small amount of krypton atoms can be observed near the surface since the temperature increased under the impact of spark discharges and caused partial thermal desorption.

It is noteworthy that the autoradiograms obtained using ^{85}Kr and ^{55}Fe are almost similar starting from the depth of ~10 μm, since atoms of both krypton and iron are uniformly distributed in the planes parallel to the surface. That is, migration of both elements occurs in three dimensions, which causes formation of a krypton solid solution in iron distributed mainly in the grain volume. The distribution of inert gas atoms completely differs from that of intrinsic atoms at a smaller depth from the surface and on the surface itself (Fig. 11). Thus, krypton atoms accumulate in gas-filled pores with a diameter of up to 2–3 μm caused by treatment, and iron atoms are located on pore walls, at the boundaries and in the volume of grains. No krypton atoms are found inside grains.

The same regularities can be observed in the autoradiograms of iron treated by an iron anode in an argon medium, which is recorded using the activation method. Localization of metal atoms and inert

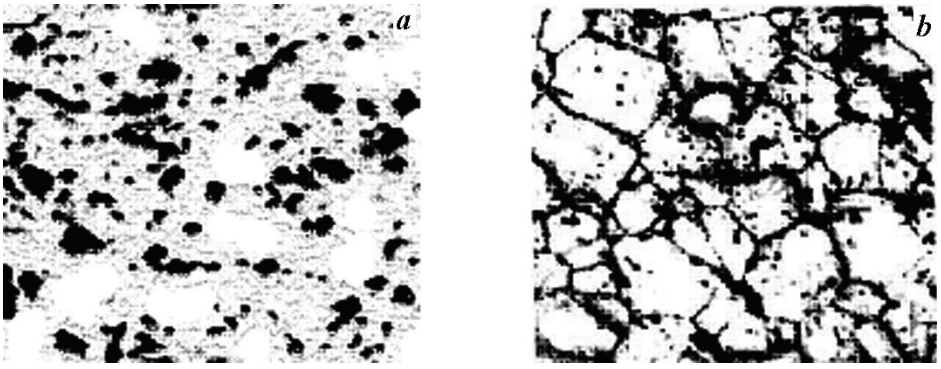

Fig. 11. *Distribution of ^{85}Kr atoms (a) and ^{55}Fe atoms (b) in iron, W=0.9 J, τ_I=200 μs, τ=1 min, l_{EG}=0.5 mm, microautoradiograms are recorded from the plane parallel to the surface, at a depth of 3 m?m, x 700 magnification*

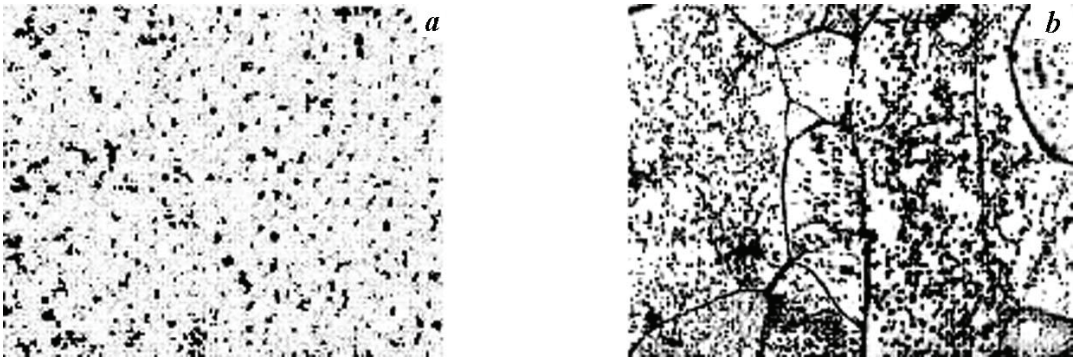

Fig. 12. *Distribution of ^{41}Ar atoms (a) and ^{55}Fe atoms (b) in iron, W=0.9 J, τ_I=200 μs, τ=1 min, l_{EG}=0.5 mm, microautoradiographs are recorded from the plane parallel to the surface, at a depth of 15 μm, x 1.000 magnification*

gas atoms is different near the surface and atoms of both elements are uniformly distributed in the grain volume at depths ≤10 μm (Fig. 12).

Let us consider simultaneous penetration of metal atoms and air gases into the base metal and the coating formation through the example of iron treatment with a molybdenum anode. The analysis of the concentration profiles of the distribution of labeled atoms ^{99}Mo in iron and in molybdenum, which penetrate from a pre-deposited iron layer of the radioactive isotope during spark doping, showed that the profiles could not be described by a simple exponential dependence since they were characterized by the presence of at least one concentration maximum for each discharge energy *W*. As the value of *W* grows, these maxima were found at greater depths (Fig. 13). The maximum concentration was found almost on the surface at *W*=0.3 J, and the maximum C_{max} shifts to the depth of the base metal by approximately 15 μm at *W*=6.4 J. However, the dependence *C*=*f*(*X*) for all values of *E* can be approximated by an exponential dependence on depth, both in the base metal and in the coating material beyond the near-surface layer. In addition to the maximum position, energy growth causes an increase in the penetration depth of molybdenum atoms in iron and in the thickness of the formed coating by a factor of 1.5 and 2, respectively. Similar results were obtained when using labeled iron atoms deposited on the sample to make a layer with a thickness of ~1 μm prior to treatment. The maximum concentration of labeled iron atoms in molybdenum at *W*=6.4 J shifts by about 15 μm. The penetration depth of ^{55}Fe atoms into iron and the thickness of the molybdenum formed coating undergo a 1.7- and 2.5-fold increase, respectively, in case *W* is changed by a factor of ~20.

In addition to the mutual penetration of metals, atoms from the medium enter the coating and the substrate. Thus, the activation autoradiography revealed the presence of nitrogen, oxygen, argon and some traces of carbon. Inert gas atoms were found in pores with the diameter of up to 1 μm located in the grain volume and in the solid solution. Nitrogen was predominantly found in the form of a solid solution, and a small amount of nitrides was observed at grain boundaries. Oxygen was uniformly distributed in the matrix. It is interesting that no intermetallic phases were observed in the diffusion zone. However, a small amount of Fe_xMo_{1-x} was detected in addition to solid solutions when a thin layer of molybdenum was deposited on iron in the area of ~2,000 nm from the surface. That was insufficient to determine the symmetry of the given compound and to compare the compound with Fe_2Mo intermetallide (λ-phase). Similar treatment of the initial thin-film (~1000 nm) electroplating coating of $_{57}$Fe located on monocrystalline molybdenum with a molybdenum anode results in the formation of an iron solid solution in molybdenum and a Fe_xMo_{1-x} intermetallic compound on the surface, where x<0.66. The molybdenum solid solution in α-Fe occurs in the form of phases with the size of up to 15 nm at a depth of ~1500 nm.

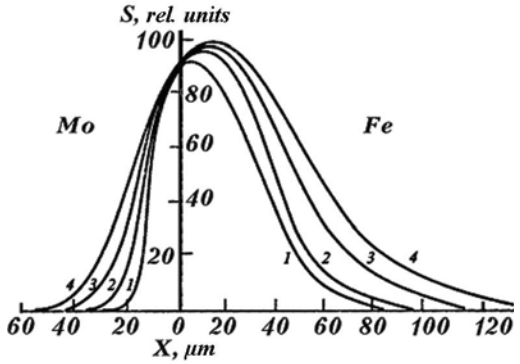

Fig. 13. *Concentration profiles of the distribution of ^{99}Mo atoms in iron and in molybdenum after ESA at energies of 0.3 J (1), 0.9 J (2), 3.1 J (3), and 6.4 J (4)*

The content of light elements in iron increases as the discharge energy grows. It is found to be comparable to the number of molybdenum atoms at *W*=15 kJ (Fig. 14).

Let us consider the interaction of steels (St.3, St.45 and St.20) with the anode material and air

gases. X-ray diffraction analysis (Table 3) and X-ray spectral analysis of molybdenum coatings on steel St.3 showed that ESA created a diffusion zone with a large number of phase components.

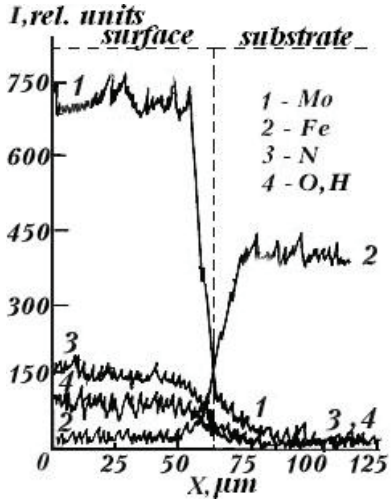

Fig. 14. *Distribution of elements in the coating and in the base metal, 15 kJ, 1 min/cm², 200 μs. Auger spectroscopy*

Table 3. *Effect of discharge energy on redistribution of phase composition in molybdenum coating on steel St.3*

Phase composition	Mo	α-Fe	α-Mo	Mo_2N	Mo_2C
Energy (*E*, J)	Relative concentration, (*C*, %)				
0.3	100	20	10	<1	<1
0.9	100	4	12	10	<1
3.1	100	0	15	15	<1
6.4	100	0	15	15	1

The diffusion zone comprises solid solutions of iron and carbon in molybdenum and nitrogen in iron, a small amount of interstitial solid solutions of nitrogen and carbon in molybdenum and nitrogen in iron, interstitial phases (molybdenum nitrides and carbides) and traces of iron nitrides (Fe_4N, Fe_2N) in addition to the initial molybdenum, a solid solution of carbon in iron and cementite (in a smaller amount due to its partial decomposition) at low values of the discharge energy only. The coating thickness increases as the discharge energy grows, which is evidenced by the decreased intensity of the diffraction maxima of iron and the increased concentration of molybdenum nitrides, while the amount of carbides varies insignificantly (Table 4).

This difference may be due to different mechanisms of phase formation – the occurrence of nitrogen in the coating is associated with its capture from ambient air during ionization of N_2 molecules in the spark discharge plasma, whereas the entrance of carbon atoms is limited by carbon concentration in steel. Indeed, when steel St.3, which comprises a smaller amount of carbon, is treated in the same mode, the diffusion zone exhibits traces of Mo_2C at E=6.4 J only. The diffraction maxima corresponding to this phase are of the background level at lower energies. Molybdenum carbides are not detected by X-ray diffraction method during the interaction of molybdenum with iron. The absence of iron nitrides in treatment with the discharge energy exceeding 0.3 J is due to the fact that nitrogen atoms do not have time to penetrate into the base metal to gain the amount sufficient for nitride formation as the thickness of the coating increases. The concentration of the nitrogen solid solution in iron becomes insignificant at E=0.9 J, even when the molybdenum anode is used to treat iron containing with no carbon atoms. This can prevent penetration of atoms of other elements during pulsed processing. It should be noted that an increase in the discharge energy causes greater homogenization of all the phases formed. Thus, the diffraction maxima shown in the X-ray diffraction patterns become less blurred (Fig. 15).

It should be noted that the coating of all the investigated steels and the diffusion zone do no exhibit molybdenum and iron oxides and oxygen solid solutions between the coating and the substrate at any of the discharge energies.

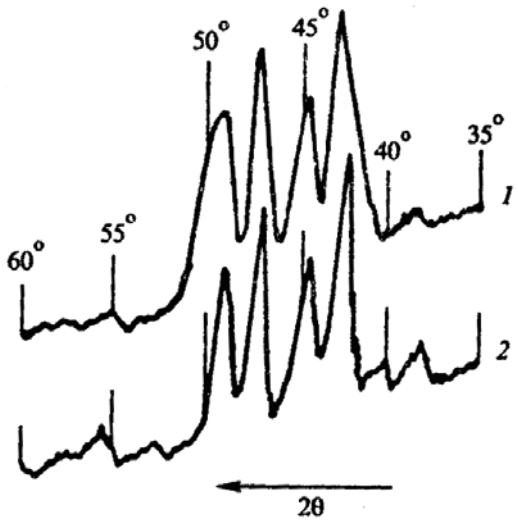

Fig. 15. *Diffraction maxima of the planes (100), (002) and (011) of the Mo_2C compound and (111) of the Mo_2N compound when treating steel St.45 with a molybdenum anode at the energies of 0.3 J (1) and 0.9 J (2).*

When the molybdenum coating (molybdenum anode) is deposited on stainless steel in ambient air, the near-surface steel layer is saturated with molybdenum and atmospheric gases. Moreover, the steel components are redistributed, and the concentration of nickel and chromium in the coating is found to be slightly higher than that in the base metal (Fig. 16). This is likely due to the occurrence of gradients in the concentration of steel components during the formation of the molybdenum coating, i.e. when metal with no chromium and nickel in its composition occurs at any time of treatment.

Table 4. *Phase composition of molybdenum coatings on steel St.20 at different spark discharge energies*

0.3 J				0.9 J			
d/*n*, nm	(hkl)	Phase	*I*, %	*d*/*n*, nm	(hkl)	Phase	*I*, %
0.260	100	Mo_2C	1	0.260	100	Mo_2C	1
0.238	002 111	Mo_2C Mo_2N	1	0.238	002 111	Mo_2C Mo_2N	1
0.222	110	Mo	100	0.222	110	Mo	100
				0.206	200	Mo_2N	5
0.202	110	Fe	20	0.202	110	Fe	5
0.157	200	Mo	30	0.157	200	Mo	30
				0.146	220	Mo_2N	3
0.147	200	Fe	5				
0.128	211	Mo	50	0.128	211	Mo	50
				0.124	311	Mo_2N	2
0.117	211	Fe	10				
0.111	220	Mo	20	0.111	220	Mo	20
0.109	220	α-Mo	10	0.109	220	α-Mo	10
0.101	220	Fe	7.5				
0.990	310	Mo	50	0.990	310	Mo	50
0.930	310	α-Mo	10	0.930	310	α-Mo	10
0.911	222	Mo	40	0.911	222	Mo	40

3.14 J				6.4 J			
d/*n*, nm	(hkl)	Phase	*I*, %	*d*/*n*, nm	(hkl)	Phase	*I*, %
0.260	100	Mo_2C	1	0.260	100	Mo_2C	1
0.237	002 111	Mo_2C Mo_2N	1	0.237	002 111	Mo_2C Mo_2N	1
0.228	011	Mo_2C	2	0.228	011	Mo_2C	2
0.222	110	Mo	100	0.222	110	Mo	100
0.205	200	Mo_2N	6	0.205	200	Mo_2N	7
0.166			3	0.166			3
0.157	200	Mo	30	0.157	200	Mo	30
0.146	220	Mo_2N	4	0.146	220	Mo_2N	4
0.128	211	Mo	50	0.128	211	Mo	50
0.124	311	Mo_2N	2	0.124	311	Mo_2N	2
				0.119	211	α-Mo	1
0.111	220	Mo	20	0.111	220	Mo	20
0.109	220	α-Mo	15	0.109	220	α-Mo	15
0.990	310	Mo	50	0.990	310	Mo	50
0.930	310	α-Mo	15	0.930	310	α-Mo	25
0.911	222	Mo	40	0.911	222	Mo	40

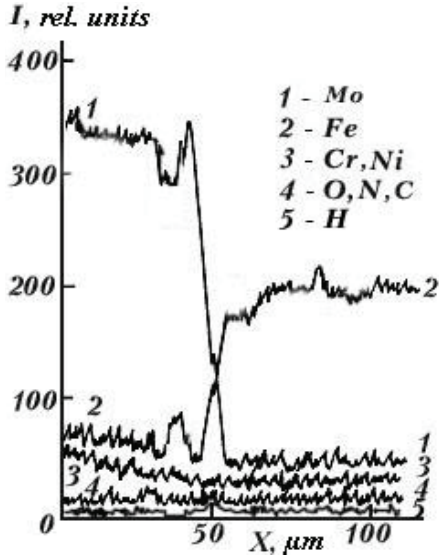

Fig. 16. *Distribution of the elements in the molybdenum coating and steel X18H10T, 15 kJ, 1 min/cm², 200 m?s. Auger spectroscopy with 0.5 μm step*

Similar phases are found to occur when depositing an iron coating (using an iron anode) on polycrystalline molybdenum. Solid solutions, iron and molybdenum nitrides, and a $Fe_{1,9}Mo$ intermetallic compound with violated stoichiometry are formed at the discharge energy *E*=6.4 J (Figs. 17 and 18). Carbide phases are not formed as it was observed in the interaction of molybdenum with steels since the amount of carbon dioxide in ambient air is insignificant as compared to nitrogen, and there are no other sources for carbon atoms to enter the coating and the base metal. In addition, oxygen atoms are found on the iron coating surface – 12 at. % of oxygen not bound to oxides. It can be assumed that oxygen occurs in the form of a supersaturated solid in iron and in molybdenum solution in α-Fe. Oxygen atoms are not found in the base metal – molybdenum – similar to the case when molybdenum was the coating material and iron was the substrate.

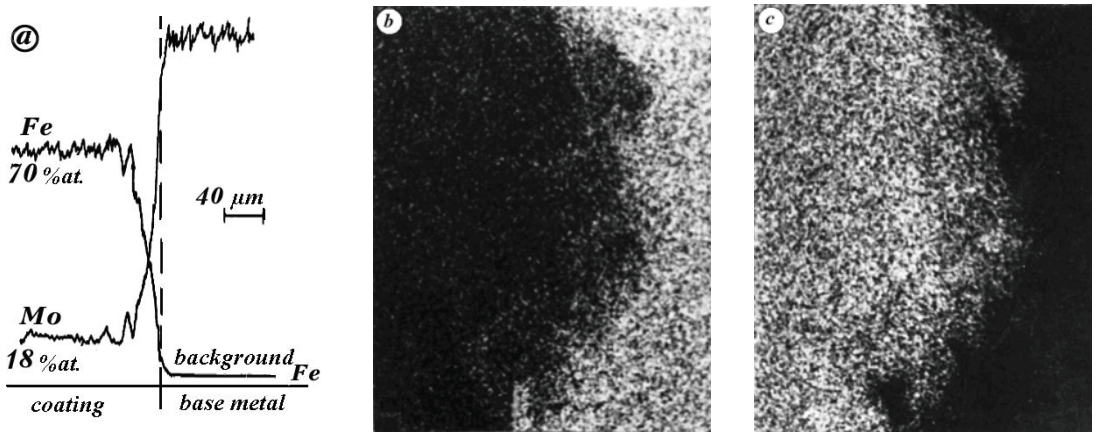

Fig. 17. *Concentration curves for the distribution of molybdenum in iron and iron in molybdenum under ESA with the discharge energy of 6.4 J (a) recorded in the reflected electrons of iron (b) and molybdenum (c), x 350 magnification*

It should be noted that the intermetallic compound is formed not on the surface of the resulting iron coating, but in the transition zone only, i.e. between the coating and the substrate. The compound occurs in the solid solution of iron in molybdenum and sprouts into the molybdenum substrate to the depth of up to 30 μm in the form of needles located normal to the surface of the molybdenum sample (Fig. 18).

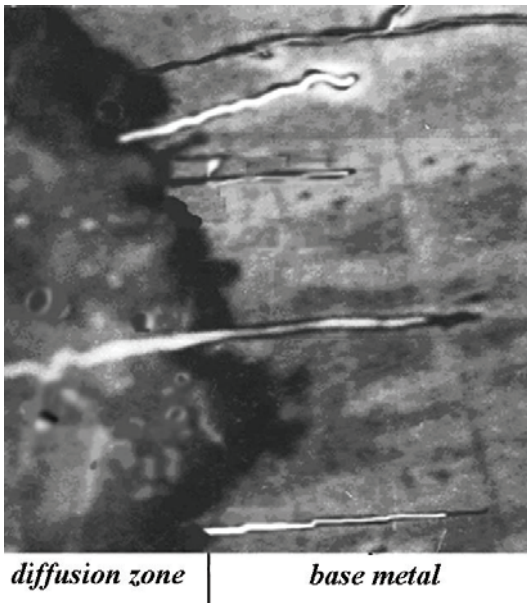

Fig. 18. *Microstructure of single-crystal molybdenum with iron coating, x 600 magnification*

When ^{99}Mo (molybdenum anode) was deposited on the molybdenum sample in different media, the following results were obtained. At W=6.4 J (1 min/cm^2, 200 μs, 0.5 mm), the depth of labeled atom penetration into molybdenum was more than 60 μm in all the media used, and the maximum concentration was found in the coating with a thickness of up to 50 μm at a distance of 5–7 μm from the interface. Beyond the maximum, there was an exponential dependence of molybdenum radioactivity on the squared penetration depth into the sample. The phase composition was different and depended on the medium in which the discharge was generated. In addition to supersaturated solid solutions of the corresponding light elements (C, N, O) and inert gases in molybdenum, there were interstitial phases, the symmetry of which corresponded to those formed under equilibrium conditions, and gas-filled pores:

Medium	N_2	NH_3	CO_2	CH_4	Ar	Kr
Phases	Mo_2N	Mo_2N	Mo_2C	Mo_2C	Pores up to 3 μm in size	

Let us note that neither a hydrogen solid solution nor hydrides were detected when using hydrogen-labeled ammonia and methane. Their formation in molybdenum was also inhibited under equilibrium conditions [33, 35]. The degree of oxygen saturation in a solid solution is much higher than that for nitrogen, carbon, argon and krypton. Thus, oxygen concentration reaches almost 10 %, while the concentration of other elements does not exceed 0.1–1 %.

Let us consider the interactions of nickel with different media. The treatment of nickel with a nickel anode in the nitrogen medium promotes the formation of a nitrogen solid solution and Ni_3N nitride, which preserves hexagonal symmetry and lattice parameters (a=0.2688 nm, c=0.4294 nm) that are characteristic of this phase under equilibrium conditions, in the matrix. Other possible nitrides Ni_4N, Ni_3N_2 and NiN_6 azide, i.e. the derivative substance formed as a result of the interaction of nickel with HN_3 nitrous acid, were not detected even in the finest near-surface layers. The autoradiogram replicas obtained under the emission of both nickel and nitrogen show reduced individual and clustered microcrystals of silver bromide uniformly distributed in the matrix mainly near grain boundaries. Moreover, the interstitial phase predominates due to low solubility of nitrogen in nickel ($2\cdot10^{-4}$ at. % under equilibrium conditions). Nevertheless, similar to the processes observed during ion bombardment in glow discharge, the solubility of nitrogen in nickel in the solid phase under spark discharge effects increases, and the maximum nickel concentration in the solid solution in the near-surface layer attains 0.1 at. %. The concentration of nitrogen in the nickel crystal lattice sharply decreases with depth, and it cannot be recorded using X-ray and radioisotope methods at the distance of ~50 μm from the surface. For the Ni_3N phase, the stoichiometric ratios do not change, but the amount of nitrides decreases, and they are not observed at the depth of up to 40 m?m. The analysis of the autoradiograms obtained at different treatment parameters (W~0.1–4.4 J, l_{EG} ~0–2 mm, τ~1–3 min/cm^2) showed that the nitrogen solid solution in nickel was typically found inside grains and nitrides were mainly located in the metal along grain boundaries (Fig. 19).

Fig. 19. *Distribution of ^{13}N in nickel after exposure to spark discharges in nitrogen medium, l_{EG}=0.5 mm, W=2.7 J, τ_I=200 μs, τ=1 min/cm^2, x 4800 magnification*

When nickel is treated with a nickel anode in ambient air, interstitial solid solutions contain nitrogen, atoms of oxygen, carbon (insignificant amount

entering from CO_2) and argon (according to the activation autoradiography data), whereas oxides are not found even on the surface (in the layer of ~200 nm). Oxygen, nitrogen, carbon and argon in the solid solution were detected using different methods; therefore, their ratio could not be determined.

The treatment of nickel with a nickel anode in ^{14}C-labeled CO_2 medium leads to formation of the concentration profile with a variable concentration of carbon in the diffusion zone over 50–75 μm at pulse energy ranging from 0.9 to 6.4 J, and to formation of a supersaturated interstitial solid solution with the maximum carbon concentration of ~3 % in the near-surface layer of up to 5 μm. The maximum carbon concentration in nickel at 1599 K does not exceed 2.7 at. % under equilibrium conditions [37]. Similar results (the maximum concentration on the surface is 3.05 at. % and the penetration depth is 78–80 μm) were obtained by ESA of nickel in a methane medium labeled with carbon. The studied interaction of nickel with carbon-labeled methane at the discharge energies ranging from 0.08 to 0.12 J showed that a solid solution with the maximum concentration ranging from ~1.8 to 1.9 at. % is formed in the near-surface layer. The lattice parameter reaches 0.3534 nm (0.3524 nm in the initial state). Despite this significant increase in the parameter, the lattice remains side-centered. The Ni_3C interstitial phases were not detected as it was in the case of isothermal annealing. As is known, this carbide can be obtained by heating through the reaction $3Ni + 2CO = Ni_3C + CO_2 \uparrow$ [32, 38].

The results of the electron microscopic autoradiography showed that labeled ^{85}Kr atoms mixed with argon caused the formation of finely dispersed gas-filled pores of ~1±3 μm in size in the diffusion zone (Fig. 20). The number and size of the pores sharply decreased with depth. Several pores were observed at the distance of up to 20 μm from the surface, whereas the solid solution of variable concentration of inert gas in nickel extended over more than 40 μm. Nevertheless, inert gas atoms virtually did not affect the mechanical characteristics of the metal starting from depths of ~10–15 μm and depending on treatment parameters. Closer to the surface, wear resistance is even smaller than that observed in treatment with pure nitrogen.

Let us consider the features of phase formation during ESA of titanium. When titanium interacts with a titanium anode in an nitrogen medium, a small amount of Ti_2N (ε-phase) with tetragonal symmetry (a=0.49343 nm, c=0.3036 nm) can be observed on the sample surface. The concentration of ε-phase increases as the treatment time grows, whereas the lattice parameters do not show significant changes. Autoradiograms of the titanium surface and two-phase titanium alloy VT 20 labeled with ^{44}Ti atoms illustrated the formation of nitrides at grain-phase interfaces. According to the activation autoradiography data obtained using ^{13}N isotope and secondary ion mass spectroscopy, nitrogen concentration decreases exponentially beyond the nitride layer (Fig. 21).

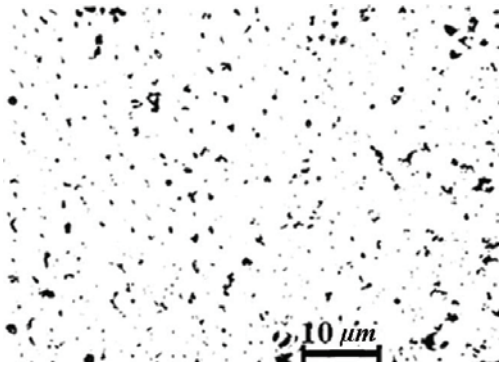

Fig. 20. *Autoradiogram replica of the nickel surface after ESA in the mixture of ^{40}Ar and ^{85}Kr, 6.4 J, 100 μs*

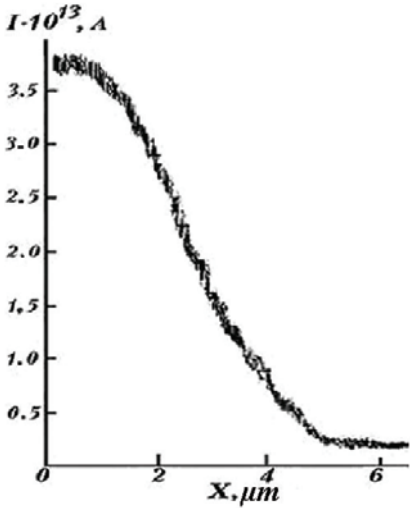

Fig. 21. *Distribution of nitrogen from the medium along the depth of the diffusion zone of titanium treated with a titanium anode (E_I=0.08 J, τ_I=200 μs, τ=10 s, l_{EG}=0.5 mm)*

It should be noted that a 6-fold increase in the treatment time, with other conditions being equal, facilitates the penetration of nitrogen atoms into titanium to the depth of 30 μm, i.e. the diffusion zone increases 5-fold. Fig. 22 illustrates the distribution of oxygen and carbon in the near-surface layers of the resulting titanium coating.

According to X-ray diffraction analysis, simultaneous saturation of the titanium surface with nickel (anode material or coating on titanium) and nitrogen (medium) causes the formation of phases in the interaction zone in the following order: nickel nitride; solid solution of nitrogen and titanium in nickel; solid solution of both alloying elements (metal and nonmetal) in titanium (Fig. 23). In this case, microhardness H_μ changes to reproduce the shape of a concentration profile of the distribution of alloying elements in titanium alloy. In the near-surface layer, H_μ

reaches ~ 1100 kg/cm^2, i.e. it exhibits an increase by the factor of ~2 and 3 in comparison with nickel and titanium, respectively.

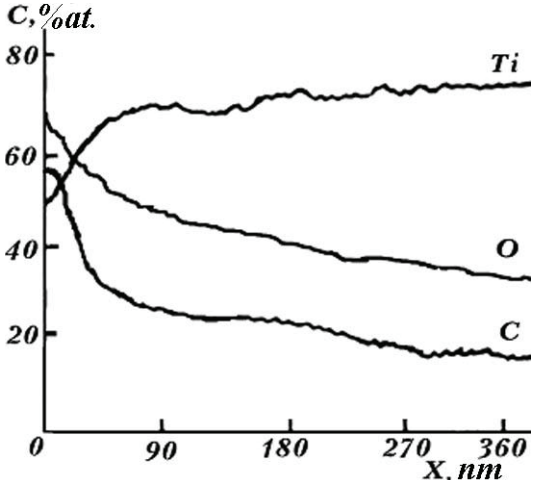

Fig. 22. *Depth distribution of oxygen and carbon entering from the medium in the diffusion zone of titanium treated with a titanium anode (E_I=0.08 J, τ_I=200 μs, τ=10 s, l_{EG}=0.5 mm)*

As the spark discharge energy increases and the treatment time grows, the depth of nickel and nitrogen penetration into titanium increases, the concentration profile and H_μ distribution decrease with the depth of more hollow profile, but the maximum values of concentration and microhardness remain virtually unchanged. Tribological tests showed that wear resistance is insignificant in the thin near-surface layer (up to X≅5–7 μm). Then, wear resistance remains virtually unchanged over 10–25 μm, and it is maximal for each ESA mode. At greater depths, wear resistance drops sharply.

Let us consider the interaction of nitrogen and carbon with titanium covered with a multicomponent coating in the initial state. The coating consists of a solid solution of phosphorus in nickel and highly-dispersed strengthening Ni_3P phase (Fig. 24).

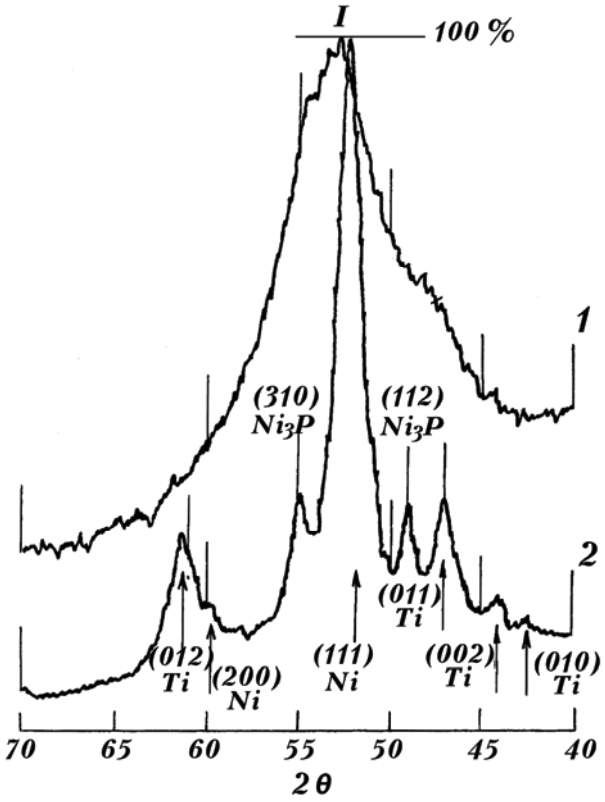

Fig. 24. *X-ray patterns of the samples with a nickel-phosphor coating on titanium in the initial state (1) and after annealing at 573 K (2), Co-radiation*

As can be seen from Fig. 24, the microstresses arising in the supersaturated solid solution of phosphorus in nickel after chemical deposition are so high that all X-ray reflections merge into one extremely broadened line. However, the shape of the diffraction maxima changes, and the X-ray patterns indicate the lines corresponding to a solid solution of phosphorus in nickel and nickel phosphide after 1-hour stabilizing annealing.

Fig. 25 illustrates the concentration curves after ESA with a nickel anode in a nitrogen medium, which indicate that the penetration depth for (X) ^{63}Ni in titanium with the initial coating and without it

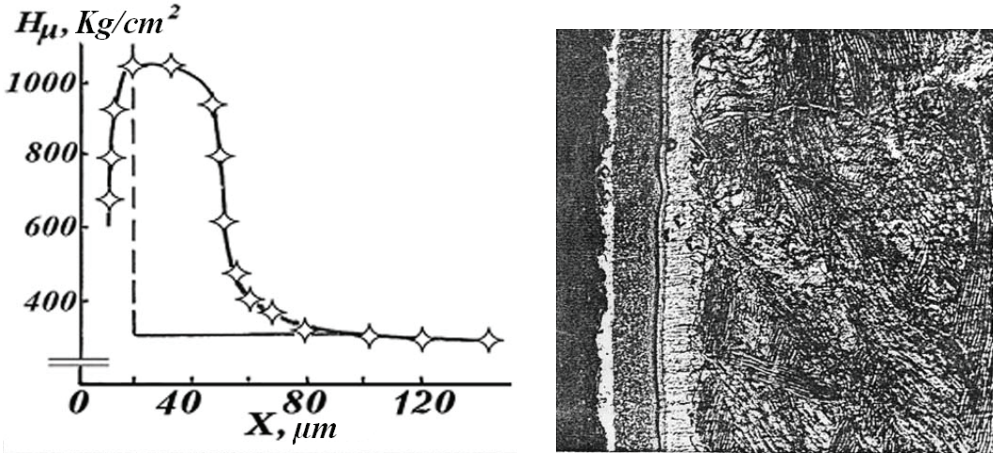

Fig. 23. *The change in microhardness throughout the depth of the diffusion zone after ESA (W=0.9 J, τ_I=200 ms*

increases as the discharge energy grows from 80 to 120 μm. A different shape of the initial section in the concentration curve (when the maximum occurs) can be observed for the samples with a coating. This can be due to the effect of the coating-substrate interface on atom redistribution.

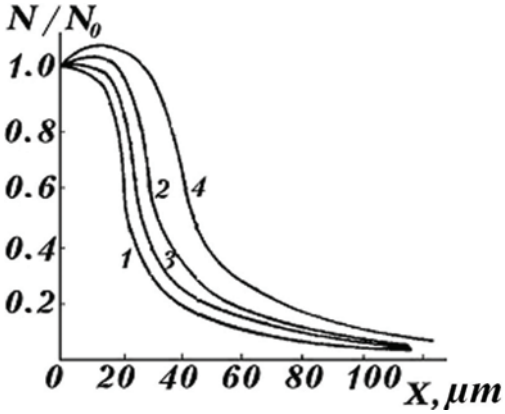

Fig. 25. *Concentration curves of ^{63}Ni distribution in titanium alloy: without initial coating at W=0.9 J (1), at W=3.14 J (2), with initial coating at W=0.9 J (3), at W=3.14 J when treated in a nitrogen medium (4)*

It should be noted that the changed phase composition of the initial coating caused by annealing does not affect the shape of the concentration profile. The analysis of the shape of the concentration profiles beyond the maximum limits shows that the change in the concentration can be best described by the exponential dependence on depth. The gradual change in nickel concentration in titanium with depth indicates the absence of intermetallic phases formed in the Ni-Ti system at temperatures above 673 K [33]. It may be concluded that the transfer of the matter (Ni-Ti) beyond the limits of the thin near-surface layer (up to 20 μm) occurs at T<673 K due to the rapid heat removal, which is characteristic of this treatment method. This indicates a diffusive character of the matter transfer under ESA. However, the observed penetration depths are much greater than those observed for diffusion under steady-state conditions at pre-melting temperatures [39] and are commensurable with the effects arising from other types of pulsed processing in the solid phase [40].

The study of the features of interaction of titanium with a nickel-phosphor coating with alloying elements (N, C) during spark alloying with anodes made of nickel and chromium or heat-resistant alloys based on these alloying elements (N, C) during spark alloying showed that phase composition of the resulting layers does not depend on whether the initial coating contained a supersaturated solid solution or two-phase state (Fig. 26, curve 1; Fig. 27, curve 1). Thus, emission of excess phosphorus from the nickel crystal lattice occurs during ESA, i.e. within several seconds, whereas this process requires at least 1 hour in isothermal annealing. Therefore, atoms of both the basic material and alloying impurities exhibit increased mobility. Thus, the previously noted non-effect of the coating state on the distribution of atoms throughout the penetration depth is due to the accelerated change in the phase composition in the initial coating under ESA.

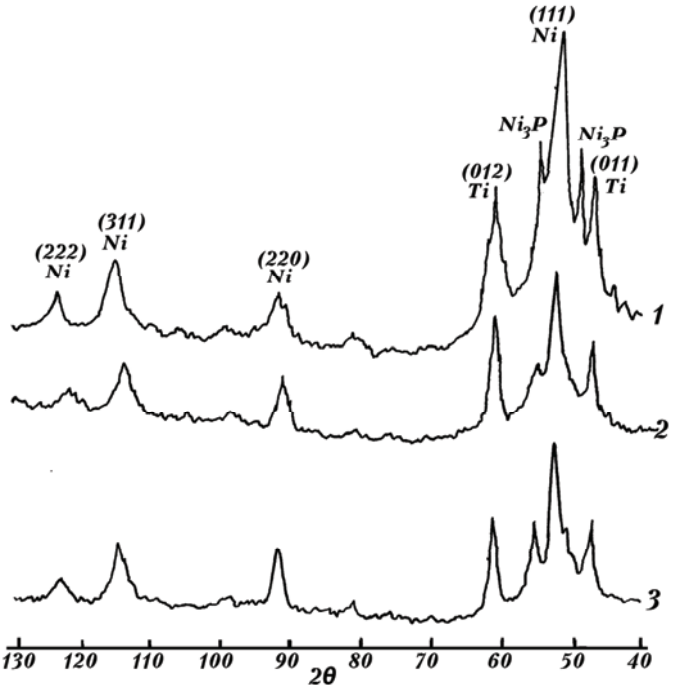

Fig. 26. *X-ray patterns of the titanium samples with a nickel-phosphor coating after annealing (1), after alloying with nickel in CO_2 medium with energies of 0.9 J (2) and 3.14 J (3), Co-radiation*

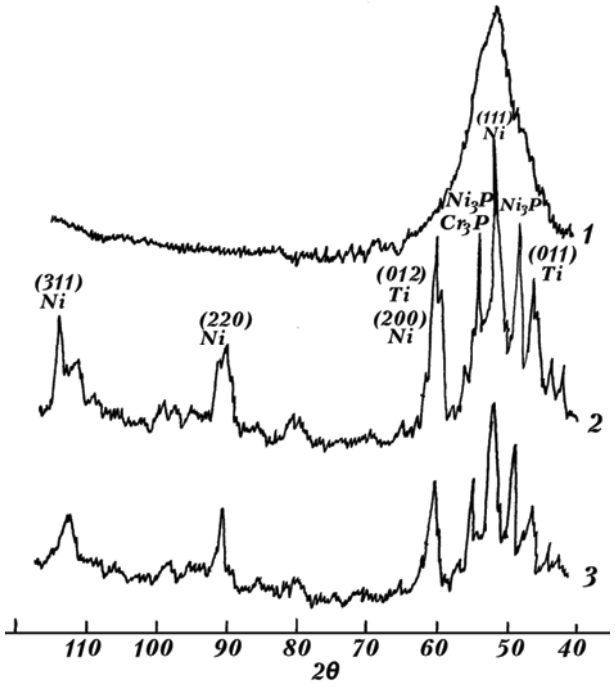

Fig. 27. *X-ray diffraction pattern of the titanium sample with a nickel-phosphor coating in the initial state (1) after alloying with chromium in nitrogen medium with the energies of 0.9 J (2) and 3.1 J (3), Co-radiation*

When carbon is incorporated from the medium, a solid solution of carbon and titanium occurs in the existing phosphorus solution in nickel. A solution of carbon and titanium in nickel, and a portion of carbon and titanium atoms from the substrate enter nickel phosphide. The coating and the diffusion zone do no exhibit new interstitial phases.

When nickel is alloyed in a nitrogen medium, mutual diffusion of nickel and titanium in the sample layers adjacent to the coating causes their mutual dissolution and formation of Ni_3N and TiN. Partial decomposition of Ni_3P and binding of phosphorus to solid solution with nickel entering the coating from the anode are observed in the strengthening phase of nickel phosphide. In addition, a portion of nitrogen atoms enters the solid solutions and dissolve in nickel phosphide.

Alloying with a nickel-chromium heat-resistant alloy leads to similar results – disappearance of all the reflections except for those corresponding to the solution of the alloying elements and titanium in nickel. At the same time, when chromium atoms are introduced, the interaction zone exhibits some amount of Ni_3P. This is evidenced by the ratio of the curve intensities (200) in K_α and K_β – radiation exceeding 1:13, which is characteristic of the absence of the other phase superposition. Apparently, chromium partially dissolves in the solid solution of nickel and phosphorus, and some amount of chromium penetrates into the Ni_3P compound (a=0.9012 nm, c=0.4422 nm), dissolving in it or displacing nickel atoms to form the Cr_3P compound, which has the same symmetry (tetragonal body-centered lattice) but slightly different parameters of the lattice if compared to nickel phosphide. The lattice parameters for Cr_3P are as follows: a=0.9185 nm and c=0.4560 nm.

In alloying with carbon and nitrogen (carbon anode, nitrogen medium), solid solutions of NiTi-C and Ti-N are formed, as well as carbides and Ti_2N titanium and Ni_3N nickel nitrides. The symmetry of the resulting phases remains unchanged, but stoichiometric ratios change in the interstitial phases – excess of metals can be observed in all the cases.

Similar to the interaction of iron and molybdenum, interaction of titanium with an initial nickel-phosphorus coating with nitrogen and carbon dioxide causes an increase in homogeneity of interstitial solid solutions of titanium and nickel at increased discharge energy (Figs 26 and 27, curves 2 and 3). A similar result of phase homogenization can be observed when using anodes made of a nickel-chromium heat-resistant alloy and chromium in both nitrogen medium and ambient air.

4. Conclusions

Thus, different methods of physico-chemical analysis showed that spark discharge alloying of metals and alloys found in a different structural-phase state with impurities is always affected by penetration of gases from the medium in which the treatment is performed. This must be taken into account since the composition and therefore the properties of the surface layer differ from those required. This can be used to create a required composition and properties of products as this paper reviews many structural materials and industrial modes of spark discharge treatment.

References

[1] Ingram D.C., Armour D.G. High dose implantation of Xe into Ni. *J. Nucl. Mater,* 1982, vol. 194, no. 1–3, pp. 117–119.

[2] Gertsriken D.S., Tyshkevich V.M., Yurik T.V. Krypton migration in aluminium under irradiation in glow discharge plasma. *Metallofizika,* 1990, vol. 12, no. 5, pp. 45–48.

[3] Gertsriken D.S., Tyshkevich V.M., Yurik T.V. Caesium diffusion in an FCC metals. *Metallofizika*, 1990, vol. 12, no. 1, pp. 55–57.

[4] Gurevich M.E., Zhuravlev A.F., Krushinskaya L.A., Larikov L.N. Kinetics of structural changes in near-to-surface aluminium layer irradiated with low energy argon ions. *Metallofizika,* 1990, vol. 12, no. 6, pp. 47–50.

[5] Gertsriken D.S., Mazanko V.F., Tyshkevich V.M. *et al*. Interaction of elements with iron and copper during pulse straining. *Phys. Metals,* 1995, vol. 14, no. 12, pp. 1329–1341.

[6] Koval N.N., Grigoriev S.V., Ivanov Yu.F. *et al.* Application of a low-pressure arc discharge for formation of hard diffusion surface layers. *XXIst International Symposium on Discharges and Electrical Insulation in Vacuum*, 2004, vol. 2. pp. 583–586.

[7] Arsenyuk B.B., Gertsriken D.S., Mazanko V.F., Peretyatka P.V., Mikhailov V.V. Effect of electro-spark alloying on the phase composition of molybdenum coatings on steel 20. *Metaloznavstvo ta obrobka metallov,* 2002, no. 4, pp. 3–8. In Ukrainian.

[8] Mazanko V.F., Mironov V.M., Gertsriken D.S., Peretiatku P.V. Formation of phases in metals at spark discharges processing. *Diffusion and diffusional phase transformations in alloys, Bulletin of Cherkasy State University. Physics*, 2002, vol. 37–38, pp. 209–212.

[9] Tyshkevich V.M., Gertsriken D.S., Falchenko V.M., Peretyatko P.V., Yanovich A.I. Features of the formation of multicomponent coatings on the titanium alloy VT20 in electro-spark alloying. *Visnyk Cherkaskoho Derzhuniversytetu,* 1999, pp. 16–23. In Russian.

[10] Arsenyuk V.V., Gertsriken D.S., Mazanko V.F., Peretyatku P.V., Mikhailov V.V. Investigation of phase composition of molybdenum coatings on iron and steel

with electro-spark treatment. *Dopovidi NANU,* 2000, no. 11, p. 113–116. In Ukrainian.

[11] Selinov I.P. *Isotopes.* Moscow, Nauka, 1970, 624 p. In Rus.

[12] Lederer G.M., Hollander I.M., Perlman I. *Table of isotopes.* New York, Ed. Willey*,* 1967, 820 p.

[13] Verkhoturov A.D. *Technology of ASA of metal surfaces.* Kiev, Tekhnyka, 1982, 181 p. In Rus.

[14] Gruzin P.L. Use of artificially radioactive indicators to study diffusion and self-diffusion processes in alloys. *DAN SSSR*, 1952, vol. 86, no. 2, pp. 289–292. In Russian.

[15] Bokshtein S.Z., Kishkin S.T., Moroz L.M. *Investigation of the structure of metals by radioactive isotope methods*. Moscow, Oborongiz, 1959, 92 p. In Rus.

[16] Bleecken S. Die Abbildungseigenschaften autoradiographischer Systeme: II. Lineare und nichtlineare autoradiographische Übertragung. *Zeitschrift fur Naturforschung – Section B Journal of Chemical Sciences,* 1968, vol. 23, no. 10, pp. 1350–1359. doi: 10.1515/znb-1968–1014.

[17] Bleecken S. Die Abbildungseigenschaften autoradiographischer Systeme III. Autoradiographisches Auflösungsvermögen. *Zeitschrift fur Naturforschung – Section B Journal of Chemical Sciences,* 1968, vol. 23, no. 11, pp. 1478–1495. doi: 10.1515/znb-1968–1111.

[18] Bokshtein S.Z. *Diffusion and structure of metals*. Moscow, Metallurgiya, 1973, 205 p. In Rus.

[19] Blackett N.M., Parry D.M. A new method for analyzing electron microscope autoradiographs using hypothecal grain distribution. *J. Cell. Biol*, 1973, vol. 57, no. 1, pp. 9–15.

[20] Bokshtein S.Z., Ginzburg S.S., Moroz L.M., Kishkin S.T. *Electron microscope autoradiography in metallurgy*. Moscow, Metallurgiya, 1978, 264 p. In Rus.

[21] Rogers A.W. *Practical autoradiography*. Amstersham, Amstersham Int. Ltd*.,* 1979, p. 74.

[22] Butler I.W. Wolicki E.A., Bernett M.K. Analysis of metal surface for residual grain of polishing compound. *Trans. of Amer. Nucl. Soc.,* 1970, vol. 13, no. 1, pp. 57–58.

[23] Babikova Yu.F., Minaev V.M. *Activation autoradiography*, vol. 1, Moscow, MIFI, 1978, 84 p. In Rus.

[24] Quaglia G., Weber G. Application de la methode de dosage en surface à l'aide des reactions nucleaires pour l'evaluation de l'interference surface-masse. *J. of Radioanal. Chem*., 1973, vol. 17, no. 1–2, pp. 91–100. doi: 10.1007/BF02520776.

[25] Cherepin V.T., Vasiliev M.A. *Secondary ion-ion emission of metals and alloys*. Kiev, Nauk. Dumka, 1975, 239 p. In Rus.

[26] Reed S. J.B. *Electron probe microanalysis*. London-New York-Melbourne, Cambridge University Press*,* 1975, 390 p.

[27] Mirkin L.I. *Handbook of X-ray structural analysis of polycrystals*. Moscow, Izd. Ph-m.l., 1964, 864 p. In Rus.

[28] M?ssbauer R.L. Kernresonanzfluoreszenz von Gammastrahlung in ^{191}Ir. *Z. Physik,* 1951, vol. 151, no. 2, pp. 124–143. doi: 10.1007/BF01344210

[29] Carlson T. A. *Photoelectron and Auger spectroscopy.* New York-London, Plenum press, 1980, 319 p.

[30] Goldstein J.I., Yakowitz H. *Practical scanning electron microscopy*. New York, Pergamon Press, 1978, 301 p.

[31] Kachanov N.N., Mirkin L.I. *X-ray diffraction analysis.* Moscow, Mechanical Engineering, 1960, 216 p. In Rus.

[32] Gertsriken D.S., Tyshkevich V.M. *Glow discharge and inert gases in metals.* Kiev, Academperiodika, 2006, 282 p. In Rus.

[33] Koval Yu.N., Barabash O.M. *Crystal structure of metals and alloys*. Kiev, Nauk. dumka, 1986, 599 p. In Rus.

[34] Mazanko V.F., Pokoev A.V., Mironov V.M., Gertsriken D.S., Mironov D.V., Lutsenko G.V. *Diffusion processes in metals under the action of magnetic fields and pulse deformations*, vol. 2. Moscow, Mashinostroyeniye, 2006, 310 p. In Rus.

[35] Lewitz F., Galas G., Bonnin D., Le Grand A.A. Etude par spectroscopie Mössbauer du fer (111) dans verres silicons multicoposants d'intérêt géologique. *Rew. Phys. Appl*., 1980, 15, no. 3, pp. 1169–1173. doi: 10.1051/rphysap:019800015060116900

[36] Van Diepen A.M., Popma Th.I.A. Temperature dependence of hyperfine field in amorphous Fe_2O_3. *Solid state comp*., 1988, vol. 27, no. 2, pp. 121–125. doi: 10.1016/0038–1098(78)90814–1.

[37] ASM Handbook, volume 3: Alloy Phase Diagrams. United States, ASM International, 1992. 800 p.

[38] Stepanenko O.M., Ledovskikh V.M., Reyter L.G., Ivanov S.I. *General and inorganic chemistry*, part II. Kiev, Pedagogíchna presa, 2000, 734 p. In Ukrainian.

[39] Adda I. Philibert J. *Diffusion dans les solides, vol.2.* Paris, Presses universitaires d France, 1966, 1296 p.

[40] Gertsriken D.S., Mazanko V.F., Falchenko V.M. *Pulsed treatment and mass transfer in metals at low temperatures*. Kiev, Nauk. dumka, 1991, 205 p. In Rus.

Received 04.04.2018